PHYSICAL REVIEW B **73**, 104424 (2006)

Microwave spectrum of square Permalloy dots: Quasisaturated state

M. Bailleul,[1,2,3,*] R. Höllinger,[2] and C. Fermon[1]

[1]*Service de Physique de l'État Condensé, DRECAM/DSM CEA Saclay, Orme des merisiers, 91191 Gif sur Yvette, France*

[2]*Institut für Experimentelle und Angewandte Physik, Universität Regensburg, 93040 Regensburg, Germany*

[3]*Institut de Physique et Chimie des Matériaux de Strasbourg, UMR 7504 ULP-CNRS, 23 rue du Loess BP 43, 67034 Strasbourg Cedex 2, France*

(Received 10 November 2005; revised manuscript received 21 December 2005; published 17 March 2006)

We report on an experimental and theoretical study of the spin-wave spectrum (1–20 GHz) in square Permalloy dots (30 nm thick, 3 μm wide) subjected to a saturating in-plane field (10–150 mT). By changing the pumping geometry, we could favor the excitation of modes with different spatial profiles. Spin-wave frequencies and mode profiles were estimated using both numerical calculations (a micromagnetic simulation and a diagonalization of the dynamical matrix) and approximate methods (use of a quantization condition and of a simplified micromagnetic edge potential). Comparison between the measurements and those calculations allows us to identify unambiguously up to 13 modes. Among those modes, we distinguish magnetostatic waves quantized both parallel (i) and perpendicular (ii) to the magnetization, spin-wave wells (iii), and a mode condensation feature (iv) resulting from a large density of states close to a minimum in the spin-wave dispersion.

DOI: 10.1103/PhysRevB.73.104424 PACS number(s): 75.30.Ds, 76.50.+g

I. INTRODUCTION

Spin dynamics in small ferromagnetic objects is becoming a crucial issue in several technological areas including magnetic recording, magnetic sensors, and MRAM's.[1] Indeed, fast writing of a magnetic bit is best achieved by using directly the precession of the magnetization.[1] Moreover, excited magnetization precession modes (spin waves) may produce an unwanted long-lived ringing of the magnetization.[1] Spin waves also manifest themselves directly in the high-frequency noise of magnetoresistive devices.[1,2] As a consequence, there has been in the last few years a sizable experimental effort to measure magnetization dynamics in confined geometry. Most studies were performed using optical techniques; either Brillouin light scattering (BLS) or time-resolved scanning Kerr effect microscopy (TRSKEM). The systems investigated were mostly flat elements of various shapes: stripes[3–10] and circular[11,12] and rectangular[13–20] dots. In most cases, the systems were subjected to a large quasisaturating in-plane magnetic field (we will not discuss here the few recent studies on truly multidomain magnetic configurations).

The results obtained could be described in terms of confined spin waves:[21] spin waves which would propagate in an unbounded ferromagnetic film are indeed reflected when they meet the physical edge of an element, which gives rise to a set of standing waves [quantized spin-wave (QSW) modes]. In the case of an axially magnetized stripe, this results in a quite simple geometrical quantization.[3–5] The situation is more complicated in the case of transversely magnetized stripes: in order to minimize demagnetizing effects, the equilibrium magnetization adopts indeed a nonuniform distribution with unsaturated edge areas. Those areas, having a low internal field, act as potential wells for the spin waves, which give rise to a set of localized modes [spin-wave well (SWW) modes].[5–10] The case of rectangular dots has naturally been described by combining confinement effects occurring in both in-plane directions. Taking into account the inhomogeneous internal field, geometrical quantization, and edge confinement, Gubbiotti *et al.*[16] and Bayer *et al.*[20] could recently interpret the frequencies of half a dozen of modes.

In this paper, we develop further this description, taking advantage of the well-resolved spin-wave spectra we have obtained using a frequency-domain inductive technique. Although this technique was not extensively used in small-object spin dynamics studies, we show that its high-frequency resolution and its sensitivity allow one to resolve a large number of modes with different character. Moreover, indirect information on the spatial profile of the modes can be obtained by changing the spatial profile of the excitation field. To interpret the observed spectra, we combine several theoretical approaches: time-domain micromagnetics are first used to obtain a global picture of the spin-wave modes without any simplifying assumption. Approximate calculations are then used to follow the frequencies of quantized and confined spin waves over the large range of applied field used in the experiment. This description is finally refined by solving directly the eigenvalue problem governing spin-wave modes (diagonalization of the dynamical matrix), which allows one to obtain the full spin-wave manifold and identify the many degenerate modes.

The paper is organized as follows. The experimental method is described in Sec. II. The results of the time-domain micromagnetic simulation are presented in Sec. III and compared to a measurement. An approximate description of quantized spin-wave modes is given in Sec. IV, where the mode indexation is justified by comparing spectra obtained with different pumping geometries. We propose in Sec. V an approximate description of spin-wave well modes in terms of an effective micromagnetic potential. Finally, we present the results of the diagonalization of the dynamical matrix (Sec. VI) and conclude (Sec. VII). The mathematical background is described in Appendixes A and B which present, respectively, the normal-mode equations of spin-wave modes and a derivation of the power absorption associated with a given mode.

II. EXPERIMENT

The microwave spectra analyzed in this paper were obtained using a frequency-domain coplanar waveguide technique which we developed initially for propagating spin-wave spectroscopy (PSWS).[5,22] The principle of the experiment is to measure the inductance of a shorted portion of a coplanar waveguide (CPW) inductively coupled to the magnetic pattern (here dots instead of the unbounded film used for PSWS), the spin-wave modes being identified as resonance peaks in this response function. Compared to the classical cavity-based ferromagnetic resonance (FMR) technique, this method has the advantage to be broadband and the sensitivity decrease associated with the nonresonant detection is compensated by a large increase of the filling factor. Using the inhomogeneous microwave magnetic field provided by the CPW, one may probe modes which would be hidden in the case of a uniform excitation. This can be seen as a small-scale analog of the FMR inhomogeneous pumping technique,[23] where it is taken advantage of the spatial distribution of the electromagnetic field in the cavity. The use of a CPW for inhomogeneous pumping was reported recently by Crawford *et al.*[15] who could observe both a symmetric and an antisymmetric quantized spin-wave mode on 50-μm Permalloy squares using pulse-induced microwave magnetometry,[24] which is a time-domain analog of the technique we describe.

The CPW we used is represented in Fig. 1(a): it is a 900-μm-long shorted portion of a so-called "coplanar waveguide with interrupted ground plane" consisting of a 4-μm-wide center conductor surrounded by two 2-μm-wide conductors with a gap of 2 μm. We integrated such waveguides on top of two different assemblies of 3-μm side Permalloy squares: in the single-row (SR) configuration [Fig. 1(b)], the assembly is a row of 103 dots with a 3-μm gap, and the center conductor of the waveguide is roughly aligned with this row. In the double-row (DR) configuration [Fig. 1(c)], the assembly comprises two rows with 120 squares each with a 3-μm gap both between dots and between rows, and the gaps between the center and side conductors of the waveguide are roughly aligned with these two rows. In the SR configuration, the microwave magnetic field $\mathbf{h}_1$ acting on the dot is mostly in plane and roughly uniform [Fig. 1(d)] whereas the DR configuration provides both an out-of-plane field in the center of the dot and an in-plane field on the dots sides which is roughly antisymmetric about the midaxis of each of the row of squares [Fig. 1(e)]. The external field $\mathbf{H}_0$ was applied in plane, either along the axis of the CPW (orientation A) or perpendicular to it (orientation P). A total of four configurations could therefore be explored (SR-A, SR-P, DR-A, and DR-P). The classical configuration for FMR (uniform in-plane $\mathbf{h}_1$ oriented perpendicular to $\mathbf{H}_0$) is best approached in the SR-A configuration which will therefore be investigated in more detail. In this paper, we restrict ourselves to relatively high fields ($\mu_0 H_0 > 10$ mT) for which the interior of the dots is saturated. This is illustrated by the magnetic force microscopy (MFM) picture in Fig. 1(f) where the magnetization nonuniformity appears to be confined close to the two edges oriented perpendicular to $\mathbf{H}_0$ (edge curling walls similar to those of transversely magnetized stripes).[9] The microwave spectra measured on the multidomain magnetic configurations occurring for $H_0 \approx 0$ will be discussed in a companion paper.[25]

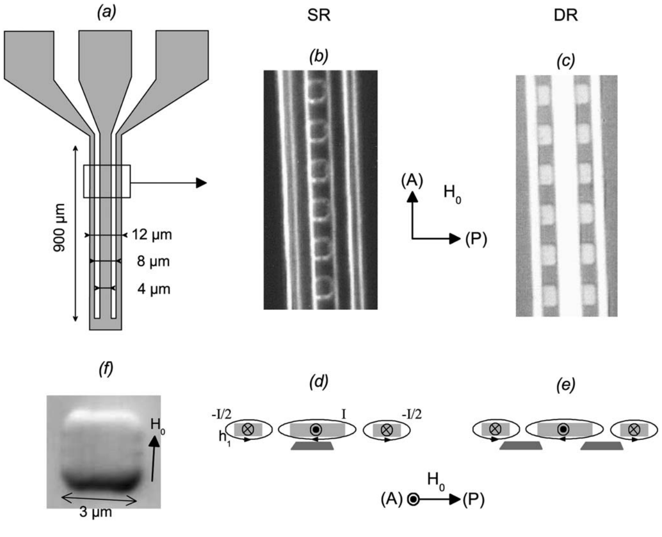

FIG. 1. (a) Sketch of the coplanar waveguide (CPW), not on scale. (b) Dark field microphotograph showing part the CPW integrated on top of the single row (SR) dots assembly. The direction of the applied field $\mathbf{H}_0$ for both configurations (*A* and *P*) is also indicated. (c) I.d. for the double row (DR) dots assembly (bright field). (d) Sketch of a cross section showing the CPW (light gray) together with the microwave current *I*, the microwave magnetic field $\mathbf{h}_1$, and a dot (dark gray) for the SR dots assembly. (e) I.d. for the DR dots assembly. (f) MFM picture of a microsquare subjected to an applied field $\mu_0 H_0 \approx 25$ mT.

The samples were fabricated as follows: a 30-nm-thick Permalloy film with a 2-nm Cr capping was first *e*-beam evaporated on a glass substrate under ultrahigh vacuum. This film was then patterned into the above-described square assemblies using optical lithography and ion-beam etching. Due to the limited resolution of optical lithography, the corners of the squares are rounded with a radius of curvature of about 300 nm [see Fig. 1(f)]. Those patterns were then covered with about 200 nm of thermally evaporated SiO for electrical isolation. Finally, the coplanar waveguides were fabricated by optical lithography (image reversal process) and lift-off of a (Ti 5 nm)/(Cu 400 nm)/(Au 10 nm) thermally evaporated trilayer. Due to the limited resolution of the optical alignment, the CPW axes are shifted about half a micron relative to the rows of dots.

Let us now describe the measurement procedure: the CPW is first connected by laying coplanar-coaxial transitions on the contact pads sketched on top of Fig. 1(a). The sample is then introduced into the gap of an electromagnet and connected to a 20-GHz vector network analyzer (Wiltron 37247A),[26] which allows one to measure the complex input impedance $Z_{11}(f,H_0)$ of each portion of the waveguide (here f is the frequency). In order to account for the impedance of the CPW itself, we first take a reference measurement

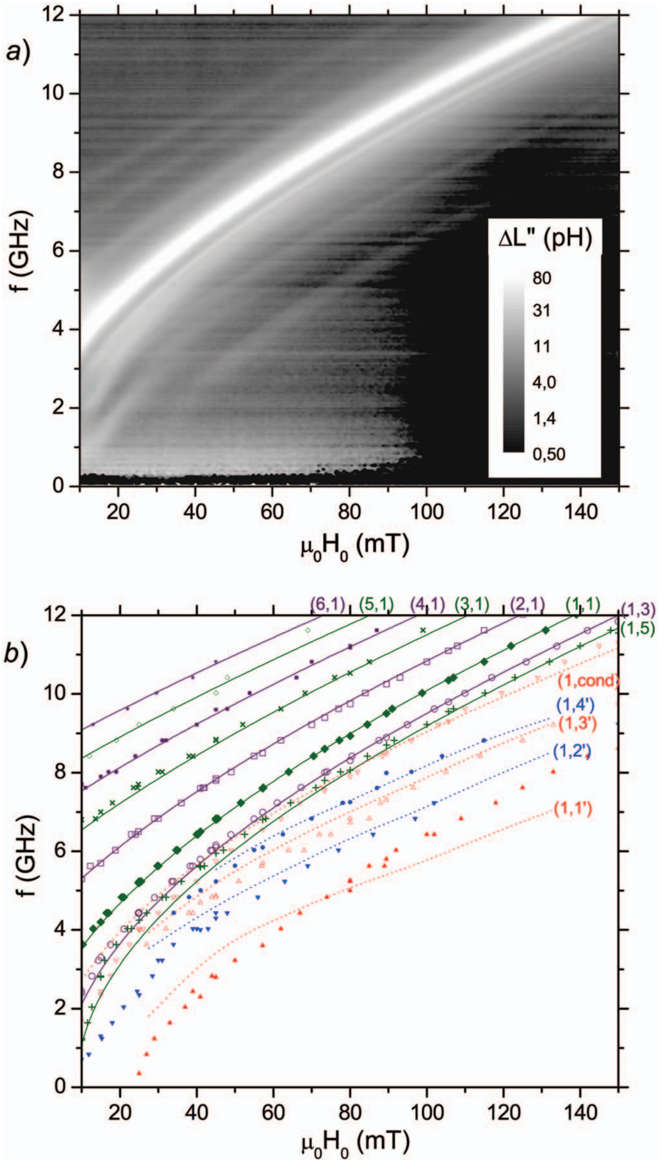

FIG. 2. (Color) (a) Gray-scale plot of the absorption spectrum for the SR-A configuration [see Figs. 1(b) and 1(d)]. (b) Locus of the mode frequencies. All the absorption peaks observed on fixed-field and fixed-frequency sweeps are gathered. The various modes identified in the next sections are displayed using different symbols and indexed using the numbers of antinodes (n_x, n_y) counted along both in-plane directions (the prime stands for edge modes). The lines are deduced from approximate calculations (see details in the next sections).

$Z_{11}(f,H_{ref})$ ($H_{ref} \simeq 800$ mT, for which the spin-wave spectra of our microsquares is expected to shift to about 35 GHz—i.e., far above the investigated frequency range). This reference is then substracted from the data to get our response function $\Delta L = [Z_{11}(f,H_0) - Z_{11}(f,H_{ref})]/2\pi f$ which is the spin-wave contribution to the self-inductance.[27] The various resonance peaks are finally identified by plotting the imaginary part $\Delta L''$ of the self-inductance change (i.e., the microwave absorption due to the spin wave modes). A typical measurement is shown in Fig. 2(a), which displays a logarithmic gray-scale plot of $\Delta L''$ as a function of applied field and frequency for the SR-A configuration.[28] Appearing as bright lines in a darker background, the various resonance modes can directly be distinguished in such a plot. The brightest line is naturally attributed to the most intense resonance which is expected to overlap the strongest with the roughly uniform pumping field. For a more detailed investigation, we can extract from this data fixed-field frequency sweeps (Fig. 3), which allow a direct comparison with a micromagnetically simulated spectrum. We can also extract fixed-frequency field sweeps (Fig. 4) which turned out to be less affected by artifacts. The absorption peaks observed on many different sweeps are gathered in Fig. 2(b). The next sections will aim at interpreting the position and intensity of these features.

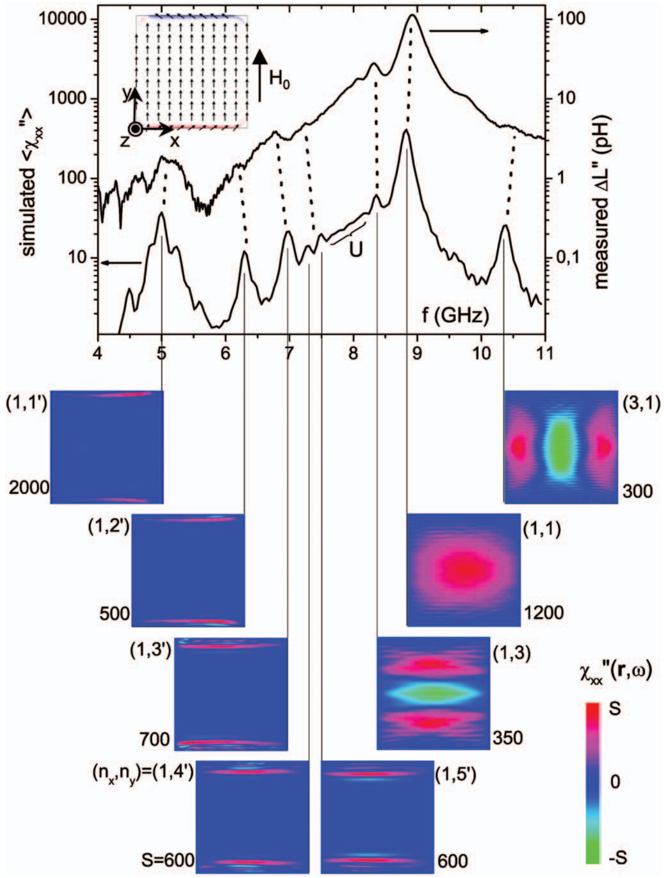

FIG. 3. (Color) Comparison between a measurement and the result of the time-domain micromagnetic simulation for an applied field $\mu_0H_0 = 80$ mT. The measured spectrum (top one) was obtained in the SR-A configuration. The simulated spectrum (bottom one) was obtained using the LLG code (Ref. 34). The equilibrium configuration and the coordinate axes are displayed as an inset (the x component of the equilibrium magnetization is represented using a blue-white-red color scale). Maps of the simulated eigenmodes are displayed below the spectra. The numbers reported on the side of each map are the mode indexation (n_x, n_y) (top) and the amplitude S spanned by the color scale (bottom).

III. TIME-DOMAIN MICROMAGNETIC SIMULATION

For a first glance, we propose in this section a full micromagnetic simulation of the response of a microsquare to an

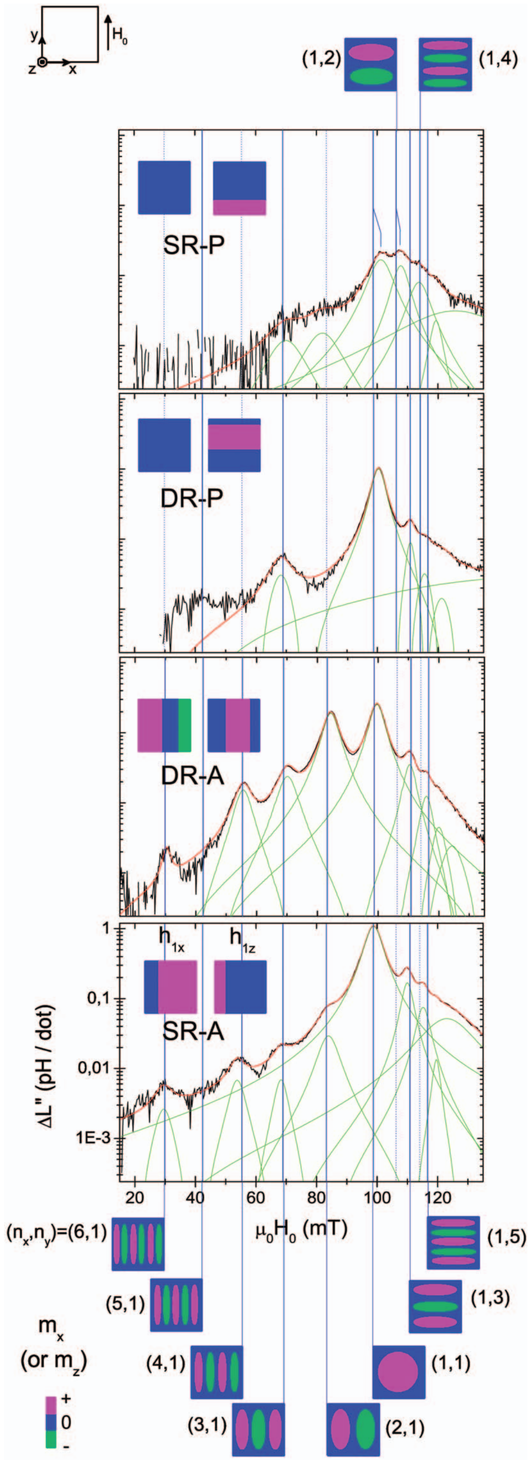

FIG. 4. (Color) Resonances measured at $f=10.02$ GHz in the four configurations described in Figs. 1(b)–1(e). The black curves show the measurements. The red curves are the result of multipeaks lorentzian fits (the green curves show the individual peaks). The resonance fields calculated using Eq. (5) are displayed as vertical blue lines (the lines become dashed ones when the excitation of the mode is forbidden due to symmetry reasons). The oscillating magnetization for the corresponding modes are sketched above and below the graphs as color maps. Sketches of the *x* and *z* component of the pumping field are also displayed as insets for each of the four configurations.

uniform exciting field for a given value of applied field ($\mu_0 H_0=80$ mT). An absorption spectrum will then be extracted from this simulation, together with maps of each of the corresponding spin-wave modes. At last, this information will be used to identify the eigenmodes responsible for the absorption measured in the SR-A configuration.

Micromagnetic simulation is now a well-established technique for the calculation of equilibrium magnetic configurations.[29] It is based on the relaxation of a discretized version of the Landau-Lifshitz-Gilbert equation [see Eq. (A1)]. While one is usually interested in the relaxed state only, it should be noted that the transient magnetization field contains all the information on spin dynamics. The most common implementation of this principle is as follows: by applying a short magnetic field pulse on a given relaxed configuration, one excites the precession of the magnetic moments. Normal modes and normal frequencies can then be deduced by Fourier transforming the simulated time evolution of the magnetization field[7,18,30–33] (an implementation based on the simulation of thermal fluctuations was also recently reported).[20]

To simulate the dynamical response of our microsquare, we use the micromagnetic code LLG.[34] The microsquare is discretized in $(10\times10\times30)$-nm^3 cells. The bias field, exchange constant and gyromagnetic ratio are set to $\mu_0 H_0=0.08$ T, $A=10^{-11}$ J m^{-1}, and $|\gamma|/2\pi=28$ GHz T^{-1} and the saturation magnetization, magnetocrystalline anisotropy, and damping constant to $\mu_0 M_s=1.13$ T, $K=0$, and $\alpha=0.005$, in agreement with spin-wave measurements on the unpatterned film.[22] In the starting configuration, the magnetization is arbitrarily saturated along the applied field (i.e., along *y*; see the inset on top of Fig. 3 where the coordinate axes used in the whole paper are defined). Then, we let this configuration relax and obtain the equilibrium configuration shown in the inset on top of Fig. 3, where the edge curling walls observed on Fig. 1(f) can be clearly distinguished. In a second step, a spatially uniform pulse field is applied along *x*, which launches the precession of the magnetization field. The pulse is 50 ps long, 1 mT high, and has a square shape (vanishing rise and fall times). In order to identify the normal modes, one then performs a Fourier transform. More precisely, we calculate the diagonal *x* term of the average susceptibility tensor of the microsquare:

$$\langle \chi_{xx}(\omega)\rangle = \frac{\langle m_x(\omega)\rangle}{\langle h_{1x}(\omega)\rangle}, \tag{1}$$

where $\langle m_x(\omega)\rangle$ $[\langle h_{1x}(\omega)\rangle]$ is the Fourier transform of the spatially averaged *x* component of the dynamic magnetization [field pulse].

The bottom curve in Fig. 3 is a semilogarithmic plot of the imaginary part of $\langle \chi_{xx}(\omega)\rangle$ (i.e., the absorption part). One clearly distinguishes eight peaks, which we attribute to the normal modes most efficiently excited by the spatially uniform pulse field. To get the spatial profile of these modes, one finally performs a local Fourier transform for each of the peak frequencies. More precisely, we calculate the diagonal *x* term of the local susceptibility tensor:

$$\chi_{xx}(\mathbf{r},\omega) = \frac{m_x(\mathbf{r},\omega)}{h_{1x}(\omega)}. \qquad (2)$$

Color plots of the imaginary part of $\chi_{xx}(\mathbf{r},\omega)$ are displayed at the bottom of Fig. 3. The zero-centered color scale may be described as follows: in the red (green) area, the magnetization is strongly excited and lags a quarter period before (after) the oscillating excitation field. On the other hand, blue designates area where the magnetization is more weakly excited. The amplitude spanned by the color scale varies from plot to plot and is reported as a factor S.

With the help of those maps, let us describe qualitatively the simulated spectrum.

(i) In the high-frequency range, one clearly distinguishes a set of three modes extending over the whole dot. Those modes are naturally interpreted as quantized spin-wave modes resulting from the geometrical confinement. They are indexed by the number of antinodes (n_x, n_y) counted along the x and y directions. It should be noted that this confinement is markedly anisotropic: (3, 1) and (1, 3) modes stand, respectively, above and below the (1, 1) peak. This feature is due to the dipole-dipole interaction: for the length scale investigated, the dipolar interaction is indeed dominant over the exchange one (so-called magnetostatic-wave regime). But this interaction is intrinsically anisotropic: two dipoles tend to orient parallel (antiparallel) when they are arranged parallel (perpendicular) to their moments. As a consequence, the dispersion of magnetostatic waves propagating in a tangentially magnetized film is markedly anisotropic:[35] the frequency of a magnetostatic wave propagating parallel (perpendicular) to the equilibrium magnetization decreases (increases) with increasing wave vector. These are the configurations referred to as magnetostatic backward volume-wave (MSBVW) and magnetostatic surface-wave (MSSW) configurations, respectively. Such an anisotropy is also expected when the spin waves are quantized, and this is what is observed in our simulation. As far as the peak intensities are concerned, it should be noted that the (1,1) mode is the most uniform one. Therefore, it couples the most strongly to the uniform field pulse and is associated with the most intense peak. Note also that the uniform field pulse couples only to modes being symmetric about the xz and yz midplanes of the dot. This explains why even QSW modes [(2,1), (1,2),…] are not observed in the simulation. A more detailed description of the QSW will be presented in Sec. IV.

(ii) In the low-frequency range, one clearly distinguishes five well-resolved peaks associated with strongly localized modes. In agreement with recent works on transversely magnetized stripes, those modes are naturally interpreted as spin-wave wells associated with the low internal field value in the edge curling walls. It is clear from the susceptibility maps that each of those modes is characterized by a different number of antinodes. Those modes will therefore be indexed $(1, n_y')$ where n_y is the number of antinodes (counted on one side of the dot only) and the prime stands for a localized feature. Those modes will be discussed in more details in Sec. V.

(iii) Finally, one also distinguishes a broad shoulder on the low-frequency side of the main resonance (around 8 GHz). This feature will be referred to as unresolved (U) and will be considered in Sec. VI.

Let us now compare the simulated spectrum to a measured one. For this purpose, the absorption measured for the SR-A configuration with $\mu_0 H_0 = 80$ mT is reported in Fig. 3 (top curve). Most of the measured peaks fall very close to the simulated ones, which allows one to unambigouously identify the (1,3), (1,1), (3,1), $(1,1')$, $(1,2')$, and $(1,3')$ peaks. The $(1,4')$ and $(1,5')$ appear to combine in a single measured peak and the U feature is measured as well. On the other hand, the 9.75-GHz peak shows up in the measured spectrum but not in the simulated one. We attribute it to the (2,1) QSW mode: contrary to the pulse field used in the simulation, the microwave field delivered by the CPW is indeed not really symmetric about the yz midplane of the dot [see Fig. 1(d)], which allows it to couple to modes with an even n_x.

As far as the resonance linewidth and line shape are concerned, it should be noted that measured high-frequency peaks are slightly broader than simulated ones. This could be attributed to a slight degradation of the Permalloy film during the patterning process (ion mill damage). On the other hand, the measured low-frequency peaks are much broader. In particular, the 6.2- and 6.7-GHz peaks nearly collapse into a single feature. We attribute this to an inhomogeneous broadening of the localized modes. The frequencies of those modes are indeed expected to depend strongly on the exact shape of the edge,[9] which very likely varies from dot to dot. Last, let us comment on the peak intensities. For this purpose, we estimate the measured susceptibility after the self-inductance change ΔL: according to the Maxwell-Ampère equation, the microwave field immediately below the center conductor is approximated as $h_{1x} = I/2w_c$ where w_c is the width of the conductor and I is the microwave current flowing in it. The contribution of the microsquares to the magnetic flux is then given by $\Delta\Phi = Ntw\mu_0\langle\chi_{xx}\rangle h_{1x}$ where N, t, and w are, respectively, the number of dots, their thickness, and their width. Thus the contribution of the microsquares to the self-inductance of the center conductor is written $\Delta L = N\mu_0(tw/2w_c)\langle\chi_{xx}\rangle$. For our SR-A sample, $N\mu_0 tw/2w_c$ is about 1 pH. The dimensionless susceptibility is therefore roughly equal to the self-inductance expressed in pH. Using this rule of thumb, one deduces from Fig. 3 a maximal measured susceptibility level of 120 to be compared to a maximal simulated susceptibility level of 500. We attribute the disagreement in part to the larger linewidth of the measured peak and in part to the pumping efficiency: the microwave field delivered by the CPW couples less to the (1, 1) normal mode than a truly uniform field would.

To conclude about this section, we have shown that dynamic micromagnetic simulations account very well for the absorption spectrum measured at $\mu_0 H_0 = 80$ mT. Moreover, the simulations provide us with maps of the eigenmodes, which allow one to identify them easily. However, such simulations are extremely time consuming. It is therefore very difficult to use them to follow the eigenmodes as a function of the applied field, as this would require a simulation for each value of H_0. For this purpose, we rather developed two approximate methods for calculating the frequencies of the QSW (Sec. IV) and SWW (Sec. V) modes.

IV. QUANTIZED SPIN-WAVE MODES

In this section, we estimate the frequencies of the QSW modes using the simplified calculation proposed by Guslienko *et al.*[36] In this approach, the normal modes are described as standing waves and their frequencies are derived from the dispersion relation for spin waves in an unbounded film. The obtained frequencies are shown to account very well for the QSW absorption peaks measured over the whole applied field range. Moreover, we discuss systematically the influence of the pumping geometry on the measured spectra.

The simplifying assumptions for the calculation are as follows: the rounding of the dots is neglected, and the equilibrium magnetization is assumed to be saturated (the edge areas have indeed little influences on the frequencies of modes extending over the whole dot). We assume that the oscillating magnetization has a sinusoidal profile in both x and y directions and that it is pinned at the edges. It may therefore be written

$$m_x(x,y) = \sin(k_x x + k_y y),$$

$$m_z(x,y) = i\epsilon \sin(k_x x + k_y y), \tag{3}$$

where ϵ is the ellipticity factor and $\mathbf{k}=k_x\mathbf{u}_x+k_y\mathbf{u}_y$ is the quantized wave vector, which is written:

$$\begin{cases} k_x = \dfrac{\pi}{w} n_x, \\ k_y = \dfrac{\pi}{w} n_y. \end{cases} \tag{4}$$

Here, (n_x, n_y) are nonzero integers which, in agreement with the indexation convention of the last section, count the number of antinodes through the sinusoidal profiles. The frequencies are then estimated by injecting the quantized wave vector into the dipole-exchange dispersion of the spin waves in the unbounded film, which is written:[37]

$$\left(\frac{\omega}{\omega_M}\right)^2 = \left(\frac{H_0}{M_s} + \frac{\langle H_{dy}\rangle}{M_s} + \Lambda^2 k^2\right)^2 + \left(\frac{H_0}{M_s} + \frac{\langle H_{dy}\rangle}{M_s} + \Lambda^2 k^2\right)[1 - P_{00}(k)\cos^2\phi] + P_{00}(k)[1 - P_{00}(k)]\sin^2\phi. \tag{5}$$

Here, $\omega_M = |\gamma|\mu_0 M_s$, $\phi=\arctan(k_x/k_y)$ is the angle between the wave vector and the applied field, $\Lambda = 2A/\mu_0 M_s^2$ is the exchange length, and $P_{00}(k)=1-[1-\exp(-kt)]/kt$ is a matrix element of the dipole-dipole interaction. $\langle H_{dy}\rangle = \int d\mathbf{r} H_{dy}(\mathbf{r}) m_x(\mathbf{r})^2 / \int d\mathbf{r} m_x(\mathbf{r})^2$ represents a space average of the static dipole field weighted by the amplitude of the oscillating magnetization.[36] This weighted average is calculated numerically, and it appears to depend only weakly on n_x but to decrease markedly as n_y increases ($\langle H_{dy}/M_s\rangle_{1,1}=-0.0058$ and $\langle H_{dy}/M_s\rangle_{1,3}=-0.0094$). This is easily understood: as the number of nodal lines perpendicular to y increases, the central area will contribute less relative to the edge areas $y\approx 0$ and $y\approx w$ (where the dipole field is strongly negative) and the averaged dipole field will therefore decrease.

The physical content of these approximations is as follows. Assuming a given profile for the eigenmode is the first step of a variational approach.[38] The deviation of the variational frequency from the true one are second order with respect to the deviation of the variational profile with respect to the true one. As they mimic qualitatively the simulated QSW of Fig. 3, sinusoidal profiles should therefore provide a satisfying ansatz for an estimate of the QSW frequencies. Guslienko *et al.* used a more complicated quantization relation than ours: they showed that the dipole-dipole interaction results in a partial pinning of the oscillating magnetization at the edges.[39] Moreover, they showed that the inhomogeneous static dipole field tends to localize spin waves in the interior of the dot.[36] To take those two effects into account, effective in-plane dimensions were introduced into the quantization relation [the dimension perpendicular (parallel) to the equilibrium magnetization is slightly increased (decreased)]. However, for the aspect ratio considered here ($w/t=100$), the dimension changes are less than 10%, which results in a resonance field shift smaller than 1 mT. This is in contrast with recent measurements on smaller dots[16,20] where those effects play a significant role. Finally, the use of Eq. (5) should also be justified. The variational approach would require one to calculate the weighted spatial average of the dynamic dipole field. By using the dispersion relation, one actually evaluates the dipole field for a periodic mode. The dipole-dipole interaction being long range, this is not expected to hold for a finite geometry. However, the error is reasonable: by calculating numerically weighted average of the oscillating dipole field, we obtained resonance fields which were less than 1 mT higher than those obtained using Eq. (5).

This method accounts very well for the positions of the measured resonances in Fig. 2(b): all of the observed high-frequency peaks appear to fall on the eight lines (green and purple plain curves) calculated using Eq. (5) and the indices (n_x, n_y) reported on the graph. To account correctly for the slopes of those curves, the material parameters had to be slightly adjusted ($\mu_0 M_s = 1.075$ T and $|\gamma|/2\pi = 29$ GHz T^{-1}), which is still in satisfactory agreement with the expected values. The key point for a proper interpretation of the locus of the resonances is the indexation of the modes. Let us now justify it in some detail. For this purpose, we compare spectra obtained in the four measurement configurations so as to get indirect information on the spatial profile of the modes. Figure 4 displays the field sweeps measured at a frequency of 10.02 GHz in the four configurations (SR-A, DR-A, DR-P, and SR-P from bottom to top). The black curve is the measured data, and the red curve is a multipeak Lorentzian fit (individual peaks are shown as green curves). The vertical blue lines are the resonance fields deduced from Eq. (5) using the indicated (n_x, n_y). The spatial profile of the oscillating magnetization for each mode is sketched at the bottom or at the top of the plots, with a color scale consistent with that of Fig. 3. The spatial profile of both components of the excitation field is also sketched as an inset for each configuration.

Let us now comment on the relative intensities of the various resonances (the intensity I is defined as the area under the corresponding individual peak in the Lorentzian fit). Qualitatively, one can see how efficiently a given mode is likely to be excited by comparing its spatial profile with that of the pumping field (see Appendix B where the equations governing the intensity of an absorption peak are derived). For a more quantitative comparison, first note that the pumping field is expected to be uniform along the axis of the CPW (the wavelength of the quasi-TEM mode propagating along the CPW is about 18 mm at 10 GHz, which ensures that the phase delay over the 900-μm-long CPW is very small). For the axial orientation of H_0, the CPW axis is to be identified with the y axis. In this case, one should therefore only excite modes which are symmetric with respect to their (xz) midplane (i.e., modes with odd n_y). Moreover, the intensity for the odd modes is expected to decrease as n_y^{-2} [this can be deduced from Eqs. (B6) and (B7) applied to a mode with a sinusoidal y profile]. This is exactly what is observed: there is no measurable peak at the positions of modes $(1,2)$ and $(1,4)$ for both SR-A and DR-A configurations. Moreover, the intensity ratios are close to the expected ones (e.g., $I_{(1,1)}^{DR\text{-}A}/I_{(1,3)}^{DR\text{-}A}=8.7\approx 3^2$, $I_{(1,1)}^{DR\text{-}A}/I_{(1,5)}^{DR\text{-}A}=24\approx 5^2$). The same observation holds for the (P) orientation where the CPW axis is to be identified with the x axis and where only modes with odd n_x are observed (the intensity ratios also follow the expected behavior—e.g., $I_{(1,1)}^{SR\text{-}P}/I_{(3,1)}^{SR\text{-}P}=8\approx 3^2$). Let us now consider the dependence of the intensities on the orientation of the pumping field. As the y component of $\mathbf{h}_1$ does not exert any torque on the magnetization in the dot center, it does not contribute to the absorption. Therefore only the x and z components matter. Using the Biot-Savart law, it can be shown that typical h_{1x} and h_{1z} fields on the plane of the dot are of the same order of magnitude. However, they contribute with very different efficiencies: in the long wavelength approximation of Eq. (A9) one obtains, from Eq. (A5) $\langle\chi_{xx}\rangle/\langle\chi_{zz}\rangle\approx[\gamma\mu_0(M_s+\langle H_{equ}\rangle)/\omega]^2$, this ratio being of the order of 9 in the present case. This is to be compared with the intensity ratio between the SR-A and DR-P configurations (which, respectively, provide roughly uniform h_{1x} and h_{1z})—e.g., $I_{(1,1)}^{SR\text{-}A}/I_{(1,1)}^{DR\text{-}P}=10.8$.

Let us now consider the effect of the profile of the pumping field in the direction perpendicular to the axis of the CPW: as this profile is neither truly symmetric nor truly antisymmetric, no selection rule strictly applies. However, the antisymmetric part of the h_{1x} field is much stronger in the DR-A configuration than in the SR-A one, which explains why the $(2,1)$ mode is so much favored in the former configuration. Moreover, the h_{1x} profile sketched for configuration SR-A extends approximately over two-thirds of the dot; it overlaps therefore very weakly with mode (3, 1) which explains the very low intensity measured for this mode. Finally, the pumping field of the SR-P configuration is peaked at one x directed edge, which explains why the intensities decrease quite slowly as n_y increases.

As a last comment in Fig. 4, it should be noted that the positions of the resonances differ slightly between each configuration. This is best seen for mode (1, 1), where the deviation largely exceeds the uncertainties on the determination of the resonance fields. We believe that this effect comes mainly from the dipolar interactions between dots. Schematically, their effect is to make the SR-A and SR-P configurations look like an axially and transversely magnetized stripe, respectively. It is well known that frequencies are higher (resonance fields are lower) in the former than in the latter case [compare, for example, the position of the main mode in Figs. 4(b) and 4(c) of Ref. 5]. From a more quantitative point of view, we have evaluated the numerically weighted space average of the in-plane dynamic and static dipole fields for assemblies of a few dots arranged as in our configurations. We found out that both static and dynamic effects combine together to increase the resonance field of mode (1, 1) in the SR-P configuration relative to the SR-A configuration by approximately 1.5 mT (while the resonance fields for the DR configurations fall in between). This is in reasonable agreement with the observed field shift. Such interaction effects were recently predicted in the case of a dense array of stripes.[40]

V. SPIN-WAVE WELL MODES

Unlike the QSW modes described above, the highly localized SWW modes are strongly dependent on the edge-equilibrium magnetic configuration. We present in this section an approximate method for determining SWW modes which relies on a careful analysis of the magnetization ground state. According to Fig. 1(f) and to the inset of Fig. 3, the nonuniformly magnetized edge areas are very elongated. In the following we will therefore neglect the x dependence of the magnetization field (i.e., we consider the case of a transversely magnetized stripe).

The starting point is the purely dipolar description by Bryant and Suhl,[41] which indicates that the edge spins tend to orient so as to create a dipole field canceling exactly the applied field in a so-called "field-free boundary zone" (FFBZ) of size s, with

$$s=\frac{tM_s}{\pi H_0}. \tag{6}$$

On the other hand, spins in the interior align with the applied field, which gives rise to a saturated zone (SZ). This picture remains valid when the exchange interaction is taken into account, except that the transition between the FFBZ and SZ becomes a smooth one.[9] The oscillation of the magnetization field around this equilibrium is governed by the combination of several restoring fields (see Appendix A): (i) the equilibrium effective field H_{equ} (which is zero in the FFBZ), (ii) the short-range exchange dynamic field $\Lambda^2\Delta\mathbf{m}$, (iii) the out of plane dipole dynamic field h_{dz}, and (iv) the in-plane dipole dynamic field h_{dy} (which is not effective in the SZ because it does not apply any torque on a y-directed magnetization). From a mathematical point of view, this problem involves both a differential operator (the exchange field) and an integral one (the dipole field), which makes it difficult to solve analytically. As suggested by Gubbiotti *et al.*,[16] the edge areas are narrow enough so that the short-range exchange field plays a dominant role. We focus therefore on the differential part of the problem and treat the integral one approximately. The modes are assumed to have the shape of a cylinder with elliptical cross section, the long and short axes being, respectively, s and t. This allows one to write $h_{dy}=-[t(t+s)]/m_y$ and $h_{dz}=-[s/(t+s)]m_z$. Let us also assume that h_{dz} dominates all other out-of-plane restoring torques. Then Eq. (A8) rewrites as an eigenvalue equation for the in-plane oscillating magnetization $m_\phi(y)$:

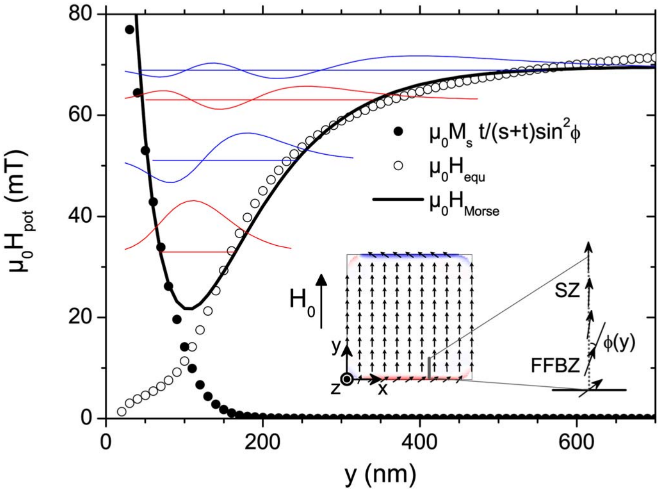

FIG. 5. (Color online) Plot of the effective potential which confines low frequency spin waves close to the edge. The data was extracted from an OOMMF micromagnetic simulation (Ref. 42) with an applied field $\mu_0 H_0 = 80$ mT. Open and solid dots are, respectively, the first and second parts of Eq. (8). The thick line is a Morse function adjusted to the total potential [Eq. (9) with parameters $\beta = 0.27$, $\delta = 0.6$, and $\sigma = 0.67$]. The horizontal lines are the eigenvalues of Eq. (7) with the Morse potential. The corresponding eigenfunctions are represented on top. The inset shows the simulation from which the data have been extracted.

$$\left(\frac{\omega}{\omega_M}\right)^2 \frac{t+s}{s} m_\phi(y) = -\Lambda^2 \frac{d^2}{dy^2} m_\phi(y) + \frac{H_{pot}(y)}{M_s} m_\phi(y), \quad (7)$$

where

$$H_{pot}(y) = H_{equ}(y) + M_s \frac{t}{s+t} \sin^2 \phi(y). \quad (8)$$

Here $\phi(y)$ is the angle between the equilibrium magnetization and the y axis. Equation (7) is similar to the Schrödinger equation for a particle in a potential. The left-hand side is to be interpreted as a total energy, the first term of the right-hand side stands for a kinetic energy, and the last term of the right-hand side plays the role of a potential energy. The second term of the "micromagnetic potential" H_{pot} is a local approximate of the effect of the dynamic in-plane dipole field.

Let us now visualize this micromagnetic potential (see Fig. 5). We use for this purpose an OOMMF micromagnetic simulation[42] with an applied field $\mu_0 H_0 = 80$ mT. The values of H_{equ} and ϕ on a short segment running normal to the edge were extracted from the relaxed state (see the inset). The two terms of the micromagnetic potential were then plotted as a function of y (open and solid circles in Fig. 5). The physical origin of the confinement becomes clear from this plot: H_{equ} tends to confine the spin waves at the edge while the in-plane dynamic dipole field tends to push them towards the interior. Those two effects combine with each other in order to form a potential well which lies between the FFBZ and the SZ. We believe that this description is more realistic than that of Ref. 16 where a fictitious saturated ground state was used.

In order to solve Eq. (7) analytically, H_{pot} is finally approximated by a Morse function

$$H_{Morse}(y) = \beta H_0 + \delta H_0 \left[1 - \exp\left(-\frac{y-y_0}{\sigma s}\right)\right]. \quad (9)$$

Here, σ and δ are dimensionless parameters describing respectively the depth and width of the potential well, β stands for the minimum of the potential, and y_0 is the location of this minimum. The eigenvalues and eigenfunctions of Eq. (7) with this potential are written[43]

$$\left(\frac{\omega_n}{\omega_M}\right)^2 \frac{t+s}{s} = \beta \frac{H_0}{M_s} + \delta \frac{H_0}{M_s}\left[1 - \left(1 - \frac{n-\frac{1}{2}}{\nu}\right)^2\right], \quad (10)$$

$$m_{\phi n}(y) = \exp\left(-\frac{\tau}{2}\right) \tau^{\nu - n + 1/2} L^{2\nu - n}_{2\nu - 2n + 1}(\tau). \quad (11)$$

Here n is an integer satisfying $1 \leqslant n \leqslant \nu + \frac{1}{2}$ where $\nu = (\sigma s / \Lambda)\sqrt{\delta H_0 / M_s}$ is an anharmonicity parameter for the potential (one recovers a harmonic potential for $\nu \gg 1$), $\tau = 2\nu \exp[-(y-y_0)/\sigma s]$ is a transformed coordinate, and $L^{2\nu-n}_{2\nu-2n+1}(\tau)$ is a generalized Laguerre polynomial. It is a polynomial of degree $n-1$ and has $n-1$ roots on the positive semiaxis (n counts therefore the number of antinodes, which is consistent with the indexation of Fig. 3).

In the case of an applied field of 80 mT, the total micromagnetic potential is best approached using $\beta = 0.27$, $\delta = 0.6$, and $\sigma = 0.67$ (the corresponding Morse potential is shown as a thick line in Fig. 5). With these values we obtain $\nu = 3.93$, which means that this potential gives rise to only four bound states. The positions of those eigenvalues are displayed on Fig. 5 as horizontal lines, on top of which are reported the profiles of the corresponding eigenfunctions. As seen for the numerically simulated edge modes (Fig. 3), those modes gradually shift towards the interior of the dot as the index increases and the modes are always dominated by the broad and intense antinode which is the furthest from the edge. Using simulations for different values of the applied field and adjusting a Morse function to each of the simulated potential, we obtained a set of eigenfrequencies which are reported on Fig. 2 as four red and blue dotted lines labeled $(1,1')$–$(1,4')$. Those estimates appear to give a satisfactory account for the four lowest-frequency resonances we have measured. It should be noted that the frequency of the $(1,1')$ clearly decreases to zero for a finite field (about 25 mT). This soft-mode behavior is attributed to a nucleation event,[9,44] which will be discussed in a companion paper devoted to the low-field data.[25]

In order to evaluate our model, let us briefly compare it with the WKB approach developed earlier to describe SWW modes. In this method, the normal mode is approximated locally as a plane wave and the mode frequency is determined by requiring the integrated phase shift to satisfy a quantization condition.[6] This method therefore involves an approximate (quasiclassical) solution, which is combined with the exact spin-wave dispersion and the micromagnetically calculated ground state to calculate eigenfrequencies.[9,10] This is in contrast with our method where exact solutions are derived from a simplified eigensytem. The strong point of our method is that it does not involve any arbitrary parameter such as the phase shift required for WKB calculations.[8,20] On the other hand, we had to make very crude approximations for evaluating the dynamic dipole field. Moreover, the exponential decay of the Morse potential does not capture completely the y^{-1} dependence of the dipole field far from the edge, which makes our approach less accurate for high index modes. Note that the eigenfunctions of Eq. (11) could be injected into a variational calculation if a more accurate evaluation of the eigenfrequencies were needed.[16]

VI. DIAGONALIZATION OF THE DYNAMICAL MATRIX

This section aims at identifying all the normal modes of the dot, in particular the quasidegenerate ones which are not resolved individually either in the measurement or in the time-domain micromagnetic simulation. This is done by discretizing the eigenvalue equation (A6) which describes the normal modes and by diagonalizing the obtained matrix (the so-called "dynamical matrix"[45]).[46] This method was recently used to interpret the spin-wave modes observed in cylindrical Permalloy dots.[48] We propose below a two- dimensional implementation together with a procedure for classifying the many calculated modes and for estimating the amount by which they contribute individually to the measured absorption. Using this procedure, we show that the unresolved U feature observed in Fig. 3 is due to the combination of several low intensity modes.

The assumptions made for the calculation are the same as those of Sec. IV: the rounding of the corners is neglected, and the equilibrium magnetization is assumed to be uniformly saturated by the y-directed 80-mT applied field. Because of this latter assumption, highly localized SWW modes will not be accurately described. However, we will see that the modes contributing to the U feature extend quite far into the interior of the dot, which makes them pretty insensitive to the details of the edge magnetic configuration. The microsquare is divided into $N=N_x\times N_y=32\times 256$ parallelepipedic cells, and the linearized Landau-Lifshitz equation (A8) is discretized, which is written

$$\frac{i\omega}{\omega_M}\begin{pmatrix} m_x(1) \\ \vdots \\ m_x(N) \\ m_z(1) \\ \vdots \\ m_z(N) \end{pmatrix} = \begin{pmatrix} & \cdots & & & \cdots & \\ \vdots & 0 & \vdots & \vdots & D_z & \vdots \\ & \cdots & & & \cdots & \\ & \cdots & & & \cdots & \\ \vdots & -D_x & \vdots & \vdots & 0 & \vdots \\ & \cdots & & & \cdots & \end{pmatrix}\begin{pmatrix} m_x(1) \\ \vdots \\ m_x(N) \\ m_z(1) \\ \vdots \\ m_z(N) \end{pmatrix}, \tag{12}$$

with

$$D_z(i,j) = \left(\frac{H_0}{M_s} + \frac{H_{dy}(i)}{M_s}\right)\delta(i,j) + K_{ech}(i,j) + K_{dzz}(i,j).$$

$$D_x(i,j) = \left(\frac{H_0}{M_s} + \frac{H_{dy}(i)}{M_s}\right)\delta(i,j) + K_{ech}(i,j) + K_{dxx}(i,j), \tag{13}$$

Here $(m_x(i), m_z(i))$ is the oscillating magnetization averaged over cell i; $H_{dy}(i)$ is the y component of the static demagnetizing field averaged over cell i. $\delta(i,j)=1$ if $i=j$ and 0 otherwise. $K_{dxx}(i,j)$ and $K_{dzz}(i,j)$ are the mutual demagnetizing factors between cells i and j (Ref. 49) and $K_{ech}(i,j)$ is a four-neighbor-exchange kernel.[50]

To save computation time, we only looked for solutions which were symmetric with respect to both the (xz) and (yz) midplanes of the dot (these are the only solutions likely to couple to an uniform excitation field such as the one used in the simulation of Sec. III). This allows one to restrict the calculation to a quadrant occupying one quarter of the dot. Equation (12) is then diagonalized using the CGEEV procedure provided in the CLAPACK package.[51] The $(N/4)$-computed positive eigenfrequencies are ordered by computing effective indices $\langle n_x\rangle$ and $\langle n_y\rangle$ which describe the degree of inhomogeneity of the corresponding eigenvectors along both x and y in-plane directions:

$$\langle n_x\rangle = \frac{N_x}{\pi}\sqrt{\frac{\sum_{q=1}^{N_x-1}\sum_{p=1}^{N_y}[m_x(\mathbf{r}_{q+1,p}) - m_x(\mathbf{r}_{q,p})]^2}{\sum_{q=1}^{N_x}\sum_{p=1}^{N_y} m_x(\mathbf{r}_{q,p})^2}},$$

$$\langle n_y\rangle = \frac{N_y}{\pi}\sqrt{\frac{\sum_{q=1}^{N_x}\sum_{p=1}^{N_y-1}[m_x(\mathbf{r}_{q,p+1}) - m_x(\mathbf{r}_{q,p})]^2}{\sum_{q=1}^{N_x}\sum_{p=1}^{N_y} m_x(\mathbf{r}_{q,p})^2}}. \tag{14}$$

In the case of the sinusoidal profiles described by Eqs. (3) and (4), $\langle n_x\rangle$ and $\langle n_y\rangle$ would reduce to the true indices n_x and n_y which count the number of antinodes along both in-plane directions. One may therefore derive from the effective indices a typical wave vector with components $(\pi/w)\langle n_x\rangle$ and $(\pi/w)\langle n_x\rangle$. Plotting frequencies as a function of the index provides an effective spin-wave dispersion. This is done in Fig. 6(a) where the eigenfrequencies are reported as a function of $\langle n_y\rangle$.

Let us first discuss the $\langle n_x\rangle$ dependence of the modes. Following the modes while their $\langle n_x\rangle$ increases, we found out that they organize themselves onto successive branches lying on top of each other. The first three branches are displayed as dots with different symbols and colors on Fig. 6(a). According to the discussion of Sec. III, these branches are attributed to MSSW standing waves with an increasing number of antinode lines (1,3,5,…). Inspection of the x profiles of some modes confirms this (not shown). Deviations of the mode profiles from a sinusoidal shape make Eq. (14) less accurate for estimating the number of antinode lines. This results in quite a broad range of $\langle n_x\rangle$ for each branch (e.g., $\langle n_x\rangle = 0.85-2.70$ for the first branch).

Let us now focus on the shape of the branches (i.e., on the $\langle n_y\rangle$ dependence of the modes). It is clear in Fig. 6(a) that each branch comprises both a cusp-forming main curve and

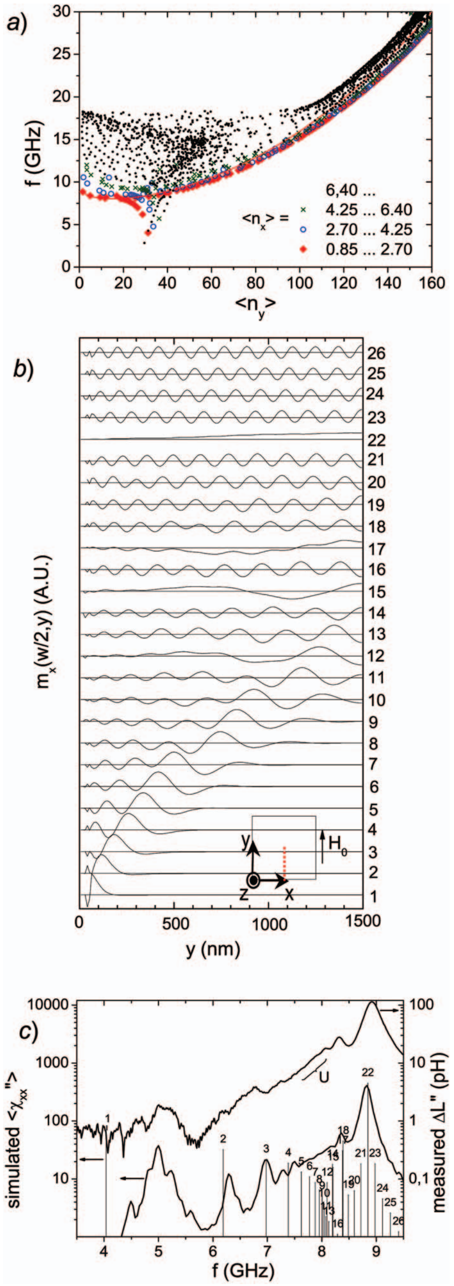

FIG. 6. (Color) Calculation of the spin-wave modes by a direct diagonalization of the diagonal matrix (see details in the text). (a) Plot of the frequencies of the symmetrical modes as a function of the effective index $\langle n_y \rangle$ (spin-wave quasidispersion). The eigenfrequencies corresponding to $\langle n_x \rangle \approx 1$, 3, and 5 are displayed as red diamonds, blue open dots, and green crosses, respectively. The red curve shows the frequency of a spin wave propagating in a continuous film with $k_x = 1(\pi/w)$, $k_y = \langle n_y \rangle \pi/w$, $\mathbf{M}_{\mathrm{equ}} \parallel \mathbf{u}_y$, and $\mu_0 H_{\mathrm{equ}} = 75$ mT. (b) y profiles of the oscillating magnetization m_x for the eigenmodes with $\langle n_x \rangle \approx 1$. (Modes are represented in increasing frequency order, from bottom to top. Only modes having the 26 lower frequencies are reported.) The profiles are taken along the dashed line shown in the inset. (c) Vertical bars show the frequencies and intensities for the 26 eigenmodes shown above [maximal susceptibility levels are deduced from Eq. (B9)]. The two spectra of Fig. 3 are reported for comparison (top curve, measurement in the SR-A configuration; bottom curve, LLG time-domain simulation).

an additional low-frequency tail. The shape of the main curve may easily be understood. Indeed, spin waves propagating along y (i.e., along the equilibrium magnetization) are expected to follow a nonmonotonic dispersion:[37] as the wave vector increases, the frequency first decreases due to the dipolar interaction (MSBVW) (Ref. 35) and then increases as the short-range exchange interaction becomes dominant. This is illustrated by the red curve in Fig. 6(a), which was deduced from Eq. (5) using Eq. (4) with $n_x = 1$ and $n_y = \langle n_y \rangle$ $[(H_0 - \langle H_{dy} \rangle)$ was set to 75 mT, which is the equilibrium field at the center of the dot]. This curve appears to reproduce fairly well the cusp-forming part of the first branch. On the other hand, we attribute the low-frequency tail to the SWW modes. This is supported by an inspection of the y profiles of the modes [see Fig. 6(b)]: modes labeled 1–9 are clearly identified as edge modes, as their intensity decays exponentially towards the center of the dot. The other modes may be divided into long-wavelength modes, corresponding to the small wave-vector dipole part of the dispersion (modes labeled 22, 17, 15, and 12 with, respectively, 1, 3, 5, and 7 antinodes along the whole dot), and short-wavelength modes, corresponding to the high-wave-vector-exchange part of the dispersion.

Figure 6(a) indicates clearly a high density of modes close to the minimum f_{min} of the spin-wave dispersion (here $f_{min} \simeq 8$ GHz). Although those strongly nonuniform modes are not expected to couple efficiently to an uniform excitation, their combination could give rise to an observable absorption feature. To check this hypothesis, we calculate the maximum susceptibility levels associated with each of the modes of Fig. 6(b), which was done using Eq. (B9) with $\alpha = 0.005$. The results of this calculation are displayed in Fig. 6(c) as vertical bars [we use the same labeling as that of Fig. 6(b)]. The measured and simulated spectra of Fig. 3 are also reported in Fig. 6(c) for comparison. Except modes labeled 1 and 2 whose frequency appear too low (this is to be associated with the assumption of a saturated magnetization, which overestimates the drop of the micromagnetic potential at the edges and therefore underestimates the frequencies of these highly localized low index SWW modes), the agreement is quite good. Indeed, modes 3, 4, 5, 17–18, and 22 account fairly well for the position of the resolved peaks. Mostly, peaks labeled 6–13 are expected to collapse into a single feature due to the finite width of the resonances ($\Delta f \approx \alpha \omega_M / 4\pi \approx 80$ MHz) and this accounts very well for the U feature (i.e., the low-frequency shoulder extending between 7.6 and 8 GHz).

This feature may therefore be seen as a “condensation of modes.” Now Fig. 6(a) indicates that the frequency f_{min} of the minimum of the spin-wave dispersion at the center of the dot provides a reasonable estimate of the position of this mode condensation. We have therefore calculated f_{min} for different values of the applied field, and we have reported it in Fig. 2(b) [red dotted line labeled (1, cond)]. This line accounts correctly for the field dependence of the U feature. Moreover, this line may be used to distinguish between edge and volume modes, which should lie, respectively, below and above it. According to this remark, we interpret the crossing of the (1, cond) and (1, 5) lines as follows: mode labeled (1, 5) actually transforms from a volume (sinusoidal in the center) to a kind of edge mode (with a weak exponential decrease toward the center) when the applied field is decreased.

VII. CONCLUSION

In this paper we reported the observation of a large number of spin-wave modes in Permalloy microsquares using a frequency-domain broadband inductive technique. Inhomogeneous pumping was used to obtain some information on the spatial profile of the modes. The positions and intensities of all these modes were interpreted by combining several theoretical approaches. A time-domain micromagnetic simulation was first Fourier transformed in order to obtain the absorption spectrum for a given value of the applied field. This allowed us to visualize two types of modes: quantized spin-wave modes extending over the whole dots and spin-wave well modes confined close to the edges oriented perpendicular to the equilibrium magnetization. Approximate methods relevant for both types of modes were then presented. QSW modes were treated with the help of a standing-wave approach. The modes were assumed to have sinusoidal profiles, and their frequencies were deduced using the spin-wave dispersion valid for an unbounded film. In order to model SWW modes, the equation governing the magnetization dynamics close to the edges was simplified into a differential equation from which exact solutions could be derived. With the help of a full diagonalization of the dynamical matrix, we also discussed how short-wavelength quasidegenerate spin-wave modes could contribute to the measured absorption. Those various methods allowed us to identify all the absorption peaks measured over the large range of applied field of the experiment [Fig. 2(b)], which is the central result of this paper. This work may be seen as a validation of several methods for interpreting spin-wave spectra, and we believe that those methods would be of particular interest for more complicated systems such as magnetic particles with a truly multidomain magnetic configuration.

ACKNOWLEDGMENTS

The authors wish to thank S. O. Demokritov and B. Hillebrands for providing the Permalloy film, M. Rastei for his help with MFM measurements, and M. Scheinfein for useful discussions. M.B. acknowledges the support from the Ecole Polytechnique and from the priority program SPP1133 “Ultrafast magnetization processes” of the Deutsche Forschungsgemeinschaft.

APPENDIX A: NORMAL-MODE EQUATIONS FOR SPIN WAVES

This appendix aims at describing the equations governing the normal modes of the magnetization field. Those are first written in the general case and then applied to a thin element with an in-plane equilibrium configuration. For pedagogical purposes, an analogy with the normal modes of vibration of a membrane is finally formulated.

The starting point is the Landau-Lifschitz-Gilbert equation, which describes the time evolution of the magnetization vector field $\mathbf{M}(r,t)$ (Ref. 29):

$$\frac{d\mathbf{M}(\mathbf{r},t)}{dt} = -|\gamma|\mu_0\mathbf{M}(\mathbf{r},t)\times\mathbf{H}_{\mathrm{eff}}(\mathbf{r},t) + \alpha\frac{\mathbf{M}(\mathbf{r},t)}{M_s}\times\frac{d\mathbf{M}(\mathbf{r},t)}{dt}, \tag{A1}$$

where γ is the gyromagnetic ratio, μ_0 is the permeability of free space, M_s is the saturation magnetization, and α is the damping constant. The first and second terms on the right-hand side of Eq. (A1) describe, respectively, a precession motion around the effective field $\mathbf{H}_{\mathrm{eff}}$ and a damping motion towards it. One usually splits the effective field into several parts corresponding to the various magnetic interactions relevant for the investigated system. In the case of our soft magnetic dots, one can neglect magnetocrystalline anisotropy and the effective field is written[29]

$$\mathbf{H}_{\mathrm{eff}}(\mathbf{r},t) = \mathbf{H}_0 + \mathbf{h}_1(\mathbf{r},t) + \mathbf{H}_d(\mathbf{r},t) + \mathbf{H}_{\mathrm{exch}}(\mathbf{r},t), \tag{A2}$$

where $\mathbf{H}_0$ is the external static uniform field, $\mathbf{h}_1$ is a small external time-dependent excitation field (optionally spatially non-uniform), $\mathbf{H}_d$ is the dipolar field, and $\mathbf{H}_{\mathrm{exch}}$ is the exchange field. The two latter ones write, respectively,

$$\mathbf{H}_d(\mathbf{r}) = (\hat{\hat{\mathbf{G}}}\cdot\mathbf{M})(\mathbf{r}) = \int d\mathbf{r}'\hat{G}(\mathbf{r},\mathbf{r}')\mathbf{M}(\mathbf{r}'), \tag{A3}$$

$$\mathbf{H}_{\mathrm{exch}}(\mathbf{r}) = \Lambda^2\Delta\mathbf{M}(\mathbf{r}), \tag{A4}$$

where

$$G_{\alpha\beta}(\mathbf{r},\mathbf{r}') = -\frac{\partial^2}{\partial x_\alpha\partial x'_\beta}\frac{1}{|\mathbf{r}-\mathbf{r}'|}$$

is the kernel of the dipolar interaction,[39] $\Lambda=\sqrt{2A/\mu_0M_s^2}$ is the exchange length, and Δ is the Laplacian operator.

When searching for normal modes of the magnetization field, one restricts oneself to small amplitude oscillations $\mathbf{m}(\mathbf{r})e^{i\omega t}$ around the equilibrium magnetization $\mathbf{M}_{\mathrm{equ}}(\mathbf{r})$. At first order, $\mathbf{m}(\mathbf{r})$ is perpendicular to $\mathbf{M}_{\mathrm{equ}}(\mathbf{r})$. Then, Eq. (A1) is rewritten[37]

$$\frac{i\omega}{\omega_M}\mathbf{m}(\mathbf{r}) = \hat{\mathbf{T}}\cdot\left(\frac{H_{equ}(\mathbf{r})}{M_s}\mathbf{m}(\mathbf{r}) - \mathbf{h}(\mathbf{r}) - \mathbf{h}_1(\mathbf{r}) + \frac{i\omega}{\omega_M}\alpha\mathbf{m}(\mathbf{r})\right). \tag{A5}$$

Here, $\omega_M=|\gamma|\mu_0M_s$ and

$$\hat{\mathbf{T}} = \begin{pmatrix} 0 & -1 \\ 1 & 0 \end{pmatrix}$$

is a matrix acting in the plane perpendicular to $\mathbf{M}_{\mathrm{equ}}(\mathbf{r})$. $\mathbf{H}_{\mathrm{equ}}(\mathbf{r})$ is the equilibrium part of the effective field [which is parallel to $\mathbf{M}_{\mathrm{equ}}(\mathbf{r})$ according to the equilibrium condition], and $\mathbf{h}(\mathbf{r})=(\hat{\hat{\mathbf{G}}}\cdot\mathbf{M})(\mathbf{r})+\Lambda^2\Delta\mathbf{m}$ comprises the dipole and exchange contributions to the oscillating part of the effective field.

Let us now write the homogeneous part of Eq. (A5) (i.e., let us drop the damping and excitation terms):

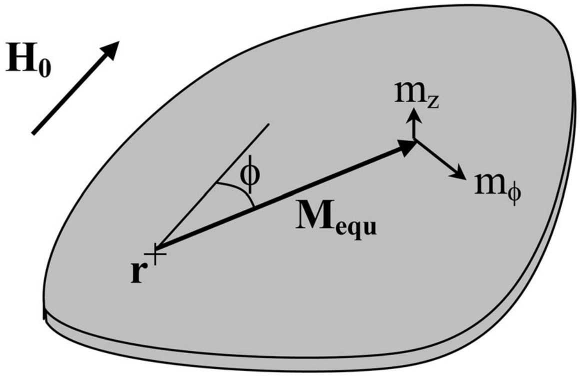

FIG. 7. Sketch of the coordinate axes used for writing the equations governing the normal modes of the magnetization field in a flat element with a nonuniform in-plane equilibrium configuration.

$$\frac{i\omega}{\omega_M}\mathbf{m} = \hat{\hat{\mathbf{D}}} \cdot \mathbf{m}, \tag{A6}$$

where $\hat{\hat{\mathbf{D}}}$ is a tensorial functional operator which is written

$$\hat{\hat{\mathbf{D}}} = \hat{\mathbf{T}} \cdot \left(\frac{H_{equ}(r)}{M_s}\mathbb{I} - \Lambda^2 \Delta \mathbb{I} - \hat{\hat{\mathbf{G}}} \right). \tag{A7}$$

Equation (A6) defines an eigenvalue problem whose eigenvalues and eigenfunctions give, respectively, the normal frequencies and normal modes of the magnetization field. For a numerical solution, Eq. (A6) can be discretized. The operator $\hat{\hat{\mathbf{D}}}$ then becomes a matrix (the so-called "dynamical matrix"),[45] which has to be diagonalized.

Let us assume the element is flat enough so that (i) the equilibrium magnetization distribution lies in the film plane[52] and (ii) both equilibrium and oscillating magnetization fields are uniform across the thickness of the element. The equilibrium configuration may therefore be described by an angle $\phi(x,y)$ measured with respect to a fixed in-plane direction and the oscillating magnetization field may be written $\mathbf{m}(x,y) = m_\phi(x,y)\mathbf{u}_\phi + m_z(x,y)\mathbf{u_z}$ (see Fig. 7). Within this approximation, it can be shown that the correlation between out-of-plane and in-plane dynamic magnetization fields vanishes. In other words, the oscillating dipole-exchange field h_z (h_ϕ) is a function of m_z only (m_ϕ only, with the additional complication that ϕ is $\mathbf{r}$ dependent). Then, writing down all the terms of Eq. (A6), one gets

$$\frac{i\omega}{\omega_M} m_\phi(\mathbf{r}) = \frac{H_{equ}(\mathbf{r})}{M_s} m_z(\mathbf{r}) - \Lambda^2 \Delta m_z(\mathbf{r}) - \int d\mathbf{r}' G_{zz}(\mathbf{r} - \mathbf{r}') m_z(\mathbf{r}'),$$

$$\frac{i\omega}{\omega_M} m_z(\mathbf{r}) = -\frac{H_{equ}(\mathbf{r})}{M_s} m_\phi(\mathbf{r}) + \Lambda^2 \Delta m_\phi(\mathbf{r}) + \int d\mathbf{r}' G_{\phi\phi'}(\mathbf{r} - \mathbf{r}') m_{\phi'}(\mathbf{r}'). \tag{A8}$$

Let us now assume that the typical wavelength of the normal mode is much larger than both the film thickness and the exchange constant. Then h_z is dominated by the out-of-plane demagnetizing field, fairly approximated in a thin-film approximation:

$$h_{dz}(\mathbf{r}) = - m_z(\mathbf{r}). \tag{A9}$$

Then, Eqs. (A8) are rewritten

$$\frac{i\omega}{\omega_M} m_\phi(\mathbf{r}) = \frac{H_{equ}(\mathbf{r})}{M_s} m_z(\mathbf{r}) + m_z(\mathbf{r}),$$

$$\frac{i\omega}{\omega_M} m_z(\mathbf{r}) = -\frac{H_{equ}(\mathbf{r})}{M_s} m_\phi(\mathbf{r}) + \Lambda^2 \Delta m_\phi(\mathbf{r}) + \int d\mathbf{r}' G_{\phi\phi'}(\mathbf{r} - \mathbf{r}') m_{\phi'}(\mathbf{r}'). \tag{A10}$$

For pedagogical purpose, let us draw an analogy between Eqs. (A10) and the equations governing the normal modes of vibration of a membrane:

$$i\omega e(\mathbf{r}) = \rho^{-1} p(\mathbf{r}),$$

$$i\omega p(\mathbf{r}) = \kappa \Delta e(\mathbf{r}), \tag{A11}$$

where $e(\mathbf{r})$ is the local out-of-plane elongation of the membrane, $p(\mathbf{r})$ is the out-of-plane momentum per unit surface, ρ is the membrane mass per unit area, and κ is the tension of the membrane.

The physical meaning of this analogy is the following

(i) The in-plane oscillating magnetization m_ϕ can be seen as a generalized position (the out-of-plane elongation in the case of the membrane).

(ii) The out-of plane oscillating magnetization field m_z appears as a generalized momentum.

(iii) The mass constant relating $i\omega m_\phi$ to m_z is the inverse of $|\gamma|\mu_0[M_s + H_{equ}(\mathbf{r})]$. In most cases (moderate applied field in large enough elements) $M_s \gg H_{equ}(\mathbf{r})$, so that the mass constant is roughly uniform.

(iv) The restoring force of the membrane is a pure curvature effect $\kappa\Delta e(\mathbf{r})$. On the other hand, the restoring force for the magnetization in a flat element comprises of three terms: an exchange term $[\Lambda^2 \Delta m_\phi(\mathbf{r})]$ playing the role of a curvature, a static effective field term $\{-[H_{equ}(\mathbf{r})/M_s] m_\phi(\mathbf{r})\}$ which plays the role of a local pressure and a dipolar term $[\int d\mathbf{r}' G_{\phi\phi'}(\mathbf{r}-\mathbf{r}') m_{\phi'}(\mathbf{r}')]$ which is a long-range counterpart of the short-range exchange curvature term.

The normal modes of vibration of a square membrane are well known: those are sinusoidal standing waves having (n_x, n_y) antinodes whose frequencies are given by $\sqrt{(\kappa/\rho)}\pi/w\sqrt{n_x^2 + n_y^2}$. As seen in this paper, the normal modes of the magnetization field in a thin element are more complicated. This is due to the two extra "restoring forces" existing in the magnetic case.

APPENDIX B: POWER ABSORPTION FOR A SPIN-WAVE MODE

This appendix aims at deriving the absorption associated to a normal mode whose spatial profile is known.

The power P absorbed by the sample is written

$$P = \mu_0 \omega \int d\mathbf{r}\, \mathrm{Im}[\mathbf{h}_1(\mathbf{r}) \cdot \bar{\mathbf{m}}(\mathbf{r})], \tag{B1}$$

where $\bar{\mathbf{m}}$ stands for the complex conjugate of $\mathbf{m}$.

Let $\{\mathbf{e_n}(\mathbf{r})\}$ be the eigenfunctions of Eq. (A6) with associated eigenvalues $\{i\omega_n/\omega_M\}$. Let a_n $[b_n]$ be the coefficients of the decomposition of $\mathbf{h}_1(\mathbf{r})$ $[\mathbf{m}(\mathbf{r})]$ onto the basis of eigenfunctions $\{\mathbf{e_n}(\mathbf{r})\}$. Then, the contribution of mode n to the absorbed power is written

$$P_n = \mu_0 \omega a_n \overline{b_n} \int d\mathbf{r} |\mathbf{e}_n(\mathbf{r})|^2. \tag{B2}$$

On the other hand, the projection of Eq. (A5) onto the eigenfunction $\mathbf{e}_n(\mathbf{r})$ is written

$$i\omega b_n \mathbf{e}_n = i\omega_n b_n \mathbf{e}_n + i\alpha\omega b_n \hat{\mathbf{T}} \cdot \mathbf{e}_n - \omega_M a_n \hat{\mathbf{T}} \cdot \mathbf{e}_n. \tag{B3}$$

Multiplying Eq. (B3) by $\bar{\mathbf{e}}_n(\mathbf{r}) \cdot \hat{\mathbf{T}}^{-1}$ and integrating over $\mathbf{r}$, one gets

$$\frac{b_n}{a_n} = \frac{\omega_M}{i\alpha\omega + \eta_n(\omega_n - \omega)}, \tag{B4}$$

where

$$\eta_n = i \frac{\int d\mathbf{r} \bar{\mathbf{e}}_n(\mathbf{r}) \cdot \hat{\mathbf{T}}^{-1} \cdot \mathbf{e}_n(\mathbf{r})}{\int d\mathbf{r} |\mathbf{e}_n(\mathbf{r})|^2}$$

is a factor depending on the ellipticity of the mode. At resonance ($\omega = \omega_n$), one gets

$$\frac{b_n}{a_n} = \frac{\omega_M}{i\alpha\omega_n}. \tag{B5}$$

Then, Eq. (B2) is rewritten

$$P_n = \frac{\omega_M}{\alpha} |a_n|^2 \int d\mathbf{r} |\mathbf{e}_n(\mathbf{r})|^2, \tag{B6}$$

where, by definition of a_n,

$$a_n = \frac{\int d\mathbf{r} \mathbf{h}_1(\mathbf{r}) \bar{\mathbf{e}}_n(\mathbf{r})}{\int d\mathbf{r} |\mathbf{e}_n(\mathbf{r})|^2}. \tag{B7}$$

This expression can be used to calculate the maximum absorption level associated with any excitation field and with any normal mode as long as both spatial profiles are known.

Let us finally write the contribution of mode n to the averaged susceptibility [Eq. (1)]:

$$\langle \chi_{xx} \rangle_n = \frac{1}{V} \frac{b_n \int d\mathbf{r} e_{nx}(\mathbf{r})}{h_{1x}}, \tag{B8}$$

where V is the volume of magnetic material. At resonance, $\langle \chi_{xx} \rangle_n$ is purely imaginary and its imaginary part $\langle \chi''_{xx} \rangle_n$ is maximum. According to Eqs. (B5) and (B7) it is rewritten

$$\langle \chi''_{xx} \rangle_n = \frac{\omega_M}{\alpha\omega_n} \frac{1}{V} \frac{\left| \int d\mathbf{r} e_{nx}(\mathbf{r}) \right|^2}{\int d\mathbf{r} |\mathbf{e}_n(\mathbf{r})|^2}. \tag{B9}$$

---

*Electronic address: bailleul@ipcms.u-strasbg.fr

[1] B. Hillebrands and K. E. Ounadjela, *Spin Dynamics in Confined Magnetic Structures* (Springer, Berlin, 2003), Vol. 2.

[2] Y. Zhou, A. Roesler, and J. G. Zhu, J. Appl. Phys. **91**, 7276 (2002).

[3] J. Jorzick, S. O. Demokritov, C. Mathieu, B. Hillebrands, B. Bartenlian, C. Chappert, F. Rousseaux, and A. N. Slavin, Phys. Rev. B **60**, 15194 (1999).

[4] Y. Roussigné, S. M. Chérif, C. Dugautier, and P. Moch, Phys. Rev. B **63**, 134429 (2001).

[5] M. Bailleul, D. Olligs, C. Fermon, and S. O. Demokritov, Europhys. Lett. **56**, 741 (2001).

[6] J. Jorzick, S. O. Demokritov, B. Hillebrands, M. Bailleul, C. Fermon, K. Y. Guslienko, A. N. Slavin, D. V. Berkov, and N. L. Gorn, Phys. Rev. Lett. **88**, 047204 (2002).

[7] J. P. Park, P. Eames, D. M. Engebretson, J. Berezovsky, and P. A. Crowell, Phys. Rev. Lett. **89**, 277201 (2002).

[8] C. Bayer, S. O. Demokritov, B. Hillebrands, and A. N. Slavin, Appl. Phys. Lett. **82**, 607 (2003).

[9] M. Bailleul, D. Olligs, and C. Fermon, Phys. Rev. Lett. **91**, 137204 (2003).

[10] C. Bayer, J. P. Park, H. Wang, M. Yan, C. E. Campbell, and P. A. Crowell, Phys. Rev. B **69**, 134401 (2004).

[11] J. Jorzick, S. O. Demokritov, B. Hillebrands, B. Bartenlian, C. Chappert, D. Decanini, F. Rousseaux, and E. Cambril, Appl. Phys. Lett. **75**, 3859 (1999).

[12] G. Gubbiotti, P. Candeloro, L. Businaro, E. Di Fabrizio, A. Gerardino, R. Zivieri, M. Conti, and G. Carlotti, J. Appl. Phys. **93**, 7595 (2003).

[13] P. H. Bryant, J. F. Smyth, S. Schultz, and D. R. Fredkin, Phys. Rev. B **47**, 11255 (1993).

[14] S. Tamaru, J. A. Bain, R. J. M. van de Veerdonk, T. M. Crawford, M. Covington, and M. H. Kryder, J. Appl. Phys. **91**, 8034 (2002).

[15] T. M. Crawford, M. Covington, and G. J. Parker, Phys. Rev. B **67**, 024411 (2003).

[16] G. Gubbiotti, M. Conti, G. Carlotti, P. Candeloro, E. Di Fabrizio, K. Y. Guslienko, A. Andre, C. Bayer, and A. N. Slavin, J. Phys.: Condens. Matter **16**, 7709 (2004).

[17] M. Cherif, Y. Roussigné, and P. Moch, Phys. Status Solidi C **1**, 1591 (2004).

[18] A. Barman, V. V. Kruglyak, R. J. Hicken, J. M. Rowe, A. Kundrotaite, J. Scott, and M. Rahman, Phys. Rev. B **69**, 174426 (2004).

[19] M. Belov, Z. Liu, R. D. Sydora, and M. R. Freeman, Phys. Rev. B **69**, 094414 (2004).

[20] C. Bayer *et al.*, Phys. Rev. B **72**, 064427 (2005).

[21] B. Hillebrands and K. E. Ounadjela, *Spin Dynamics in Confined Magnetic Structures*, (Springer, Berlin, 2001), Vol 1.

[22] M. Bailleul, D. Olligs, and C. Fermon, Appl. Phys. Lett. **83**, 972 (2003).

[23] J. F. Dillon, J. Appl. Phys. **31**, 1605 (1960).

[24] T. J. Silva, C. S. Lee, T. W. Crawford, and C. T. Rogers, J. Appl. Phys. **85**, 7849 (1999).

[25] M. Bailleul, R. Höllinger, K. Perzlmaier, and C. Fermon (unpublished).

[26] The system is previously calibrated at the coaxial ends of the coplanar-coaxial transitions using coaxial standards. The electrical delay introduced by the coplanar-coaxial transitions is taken into account by suitably offsetting the reference planes.

[27] The high-frequency phase shift due to the small capacitance of the waveguide is taken into account by a correction which is proportional to $j2\pi fC(R+j2\pi fL)$ where R, L, and C are, respectively, the total distributed resistance, capacitance, and inductance of the waveguide, evaluated by fitting the reference input impedance to a distributed *RLC* model [see Fig. 1(c) in Ref. 22 where similar CPW were used].

[28] Measurement parameters are as follows: the microwave power was reduced to −15 dBm to avoid nonlinear effects (at 0 dBm, the peaks were considerably broadened and shifted). With a 1 kHz bandwidth and 20 averagings, it required typically 1 h to obtain one full $\Delta L(f,H_0)$ spectrum. In these conditions, the intensity of the smallest peaks we can distinguish is around 1 pH. We attribute this limitation to an imperfect calibration process (resulting in a small undulation during frequency sweeps) and a mechanical drift due to weakly magnetic connectors (resulting in small slopes and steps during field sweeps).

[29] A. Hubert and R. Schäfer, *Magnetic Domains* (Springer, Berlin, 1998).

[30] O. Gerardin, H. Le Gall, M. J. Donahue, and N. Vukadinovic, J. Appl. Phys. **89**, 7012 (2001).

[31] M. Buess, R. Höllinger, T. Haug, K. Perzlmaier, U. Krey, D. Pescia, M. R. Scheinfein, D. Weiss, and C. H. Back, Phys. Rev. Lett. **93**, 077207 (2004).

[32] M. Grimsditch, G. K. Leaf, H. G. Kaper, D. A. Karpeev, and R. E. Camley, Phys. Rev. B **69**, 174428 (2004).

[33] V. Novosad, M. Grimsditch, K. Y. Guslienko, P. Vavassori, Y. Otani, and S. D. Bader, Phys. Rev. B **66**, 052407 (2002).

[34] http://llgmicro.home.mindspring.com

[35] R. W. Damon and J. R. Eshbach, J. Phys. Chem. Solids **19**, 308 (1961).

[36] K. Y. Guslienko, R. W. Chantrell, and A. N. Slavin, Phys. Rev. B **68**, 024422 (2003).

[37] B. A. Kalinikos and A. N. Slavin, J. Phys. C **19**, 7013 (1986).

[38] H. Benson and D. L. Mills, Phys. Rev. **188**, 849 (1969).

[39] K. Y. Guslienko, S. O. Demokritov, B. Hillebrands, and A. N. Slavin, Phys. Rev. B **66**, 132402 (2002).

[40] M. P. Kostylev, A. A. Stashkevich, and N. A. Sergeeva, Phys. Rev. B **69**, 064408 (2004).

[41] P. Bryant and H. Suhl, Appl. Phys. Lett. **54**, 2224 (1989).

[42] Object-oriented micromagnetic framework, www.nist.gov

[43] L. Landau and E. Lifchitz, *Mécanique Quantique* (Mir, Moscow, 1967).

[44] Y. Roussigné, S. M. Chérif, and P. Moch, J. Magn. Magn. Mater. **268**, 89 (2004).

[45] M. Grimsditch, L. Giovannini, F. Montoncello, F. Nizzoli, G. K. Leaf, and H. G. Kaper, Phys. Rev. B **70**, 054409 (2004).

[46] One should also mention a one-dimensional implementation, in which the eigenvalue integro-differential equation is directly solved (Ref. 10) and methods based on the inversion of the dynamical matrix, in which the response to a given microwave field is directly calculated (Refs. 44 and 47).

[47] S. Labbé and P. Y. Bertin, J. Magn. Magn. Mater. **206**, 93 (1999).

[48] L. Giovannini, F. Montoncello, F. Nizzoli, G. Gubbiotti, G. Carlotti, T. Okuno, T. Shinjo, and M. Grimsditch, Phys. Rev. B **70**, 172404 (2004).

[49] A. J. Newell, W. Williams, and D. J. Dunlop, J. Geophys. Res., [Solid Earth] **98**, 9551 (1993).

[50] M. J. Donahue and R. D. McMichael, Physica B **233**, 272 (1997).

[51] www.netlib.org

[52] Note that this description does not apply to vortices and Bloch walls, in which the magnetization points out of plane.